

Large thermoelectric power factor in p-type Si (110)/[110] ultra-thin-layers compared to differently oriented channels

Neophytos Neophytou and Hans Kosina

Citation: *J. Appl. Phys.* **112**, 024305 (2012); doi: 10.1063/1.4737122

View online: <http://dx.doi.org/10.1063/1.4737122>

View Table of Contents: <http://jap.aip.org/resource/1/JAPIAU/v112/i2>

Published by the [American Institute of Physics](http://www.aip.org).

Related Articles

Electronic structure and thermoelectric properties of nanostructured $\text{EuTi}_{1-x}\text{Nb}_x\text{O}_{3-\delta}$ ($x=0.00; 0.02$)
Appl. Phys. Lett. **101**, 033908 (2012)

Electrical and thermoelectric properties of single-wall carbon nanotube doped Bi_2Te_3
Appl. Phys. Lett. **101**, 031909 (2012)

Transport, thermoelectric, and magnetic properties of a dense Cr_2S_3 ceramic
J. Appl. Phys. **112**, 013716 (2012)

Origin of n-type conductivity of Sn-doped Mg_2Si from first principles
J. Appl. Phys. **112**, 013715 (2012)

Electrical and thermal spin accumulation in germanium
Appl. Phys. Lett. **101**, 022402 (2012)

Additional information on J. Appl. Phys.

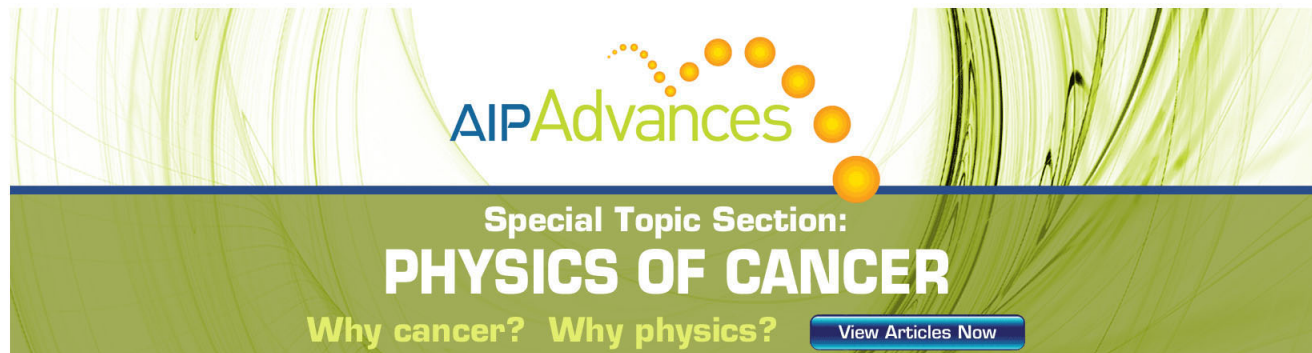
Journal Homepage: <http://jap.aip.org/>

Journal Information: http://jap.aip.org/about/about_the_journal

Top downloads: http://jap.aip.org/features/most_downloaded

Information for Authors: <http://jap.aip.org/authors>

ADVERTISEMENT

The advertisement features a green background with a pattern of thin, wavy lines. At the top, the 'AIP Advances' logo is displayed, with 'AIP' in blue and 'Advances' in green, accompanied by a series of orange dots. Below the logo, the text 'Special Topic Section: PHYSICS OF CANCER' is written in white, with 'PHYSICS OF CANCER' in a larger, bold font. At the bottom, the phrase 'Why cancer? Why physics?' is written in yellow, and a blue button with the text 'View Articles Now' is located on the right side.

AIP Advances

Special Topic Section:
PHYSICS OF CANCER

Why cancer? Why physics? [View Articles Now](#)

Large thermoelectric power factor in p-type Si (110)/[110] ultra-thin-layers compared to differently oriented channels

Neophytos Neophytou^{a)} and Hans Kosina^{a)}*Institute for Microelectronics, TU Wien, Gußhausstraße 27-29/E360, A-1040 Wien, Austria*

(Received 16 April 2012; accepted 9 June 2012; published online 18 July 2012)

Using atomistic electronic structure calculations and Boltzmann semi-classical transport, we compute the thermoelectric power factor of ultra-thin-body p-type Si layers of thicknesses from $W = 3$ nm up to 10 nm. We show that the power factor for channels in [110] transport orientation and (110) surface confinement largely outperforms all differently oriented channels by more than $2\times$. Furthermore, the power factor in this channel increases by $\sim 40\%$ with layer thickness reduction. This increase, together with the large confinement effective mass of the (110) surface, make this particular channel less affected by the detrimental effects of enhanced surface roughness scattering and distortion at the nanoscale. Our results, therefore, point towards the optimal geometrical features regarding orientation and length scale for power factor improvement in 2D thin-layers of zincblende semiconductors. © 2012 American Institute of Physics. [<http://dx.doi.org/10.1063/1.4737122>]

I. INTRODUCTION

The ability of a material to convert heat into electricity is measured by the dimensionless thermoelectric (TE) figure of merit $ZT = \sigma S^2 T / (\kappa_e + \kappa_l)$, where σ is the electrical conductivity, S is the Seebeck coefficient, κ_e is the electronic part, and κ_l is the lattice part of the thermal conductivity. Some of the best thermoelectric materials are based on rare earth or toxic elements and exhibit $ZT \sim 1$, which corresponds to low efficiencies of the order of $\sim 10\%$ of the Carnot efficiency.¹⁻³ Recent breakthrough experiments, however, have demonstrated that nanostructured and low-dimensional channels can offer large improvements in ZT compared to the raw materials' values. Such effects have been observed for 1D nanowires (NWs),^{4,5} 2D thin-layer superlattices,⁶⁻⁹ as well as materials with embedded nanostructures.^{10,11} More importantly, this has been achieved for common semiconductor materials such as Si, SiGe, and InGaAs.^{4,5,8,9}

Most of this improvement has been attributed to a remarkable reduction in the phonon thermal conductivity κ_l because of enhanced phonon scattering on the boundaries of narrow features and disorder.^{4,8,12-15} Narrow feature sizes, on the other hand, will in general degrade the electrical conductivity and power factor σS^2 as well. In order to achieve efficient thermoelectric devices, σS^2 needs to be kept high by proper optimization of the interplay between σ and S . As we showed in previous works, at the nanoscale the transport and surface orientations as well as the confinement length scale are degrees of freedom through which electronic properties can be optimized.^{16,17} The sensitivity of the electronic properties to geometric parameters is especially strong in p-type nanoscale channels.^{16,18}

In this work, we calculate the room temperature thermoelectric power factor of p-type Si ultra-thin-body (UTB) layers for thicknesses from $W = 3$ nm up to 10 nm. Such channels, but also 2D superlattices formed of thin layers of these dimen-

sions are promising candidates for TE applications.^{6-9,19} We employ atomistic electronic structure and Boltzmann transport calculations. Our analysis shows that the variations in the electronic structure of the UTB layers with confinement and orientation can provide ways for power factor optimization. We demonstrate that the power factor of the (110)/[110] p-type Si channel outperforms by more than $2\times$ the power factor for all other surface/transport orientations. In addition, we show that the power factor in this channel improves as the layer width is reduced down to 3 nm, an effect that can potentially offset the detrimental effect of enhanced surface roughness scattering (SRS) with feature scaling. Our results, therefore, offer power factor optimization routes for high performance, thin-layer thermoelectric devices as well as thin 2D superlattice thermoelectric devices. The mechanisms we describe originate from features of the heavy-hole (HH) valence band, which are common in all zincblende semiconductors, and we therefore expect that our results would be qualitatively valid for other such semiconductors as well.

II. APPROACH

We couple the 20 orbital atomistic $sp^3d^5s^*$ -spin-orbit-coupled (SO) tight-binding (TB) model²⁰ to linearized Boltzmann transport theory.²¹⁻²³ This TB model accurately describes the electronic structure and inherently includes the effects of quantum confinement and orientation. It is a compromise between computationally expensive *ab-initio*, and inexpensive but less accurate effective mass methods. The electrical conductivity σ and the Seebeck coefficient S follow from linearized Boltzmann theory as

$$\sigma = q_0^2 \int_{E_V}^{\infty} dE \left(-\frac{\partial f_0}{\partial E} \right) \Xi(E), \quad (1a)$$

$$S = \frac{q_0 k_B}{\sigma} \int_{E_V}^{\infty} dE \left(-\frac{\partial f_0}{\partial E} \right) \Xi(E) \left(\frac{E - E_F}{k_B T} \right), \quad (1b)$$

^{a)}Electronic addresses: neophytou@iue.tuwien.ac.at and kosina@iue.tuwien.ac.at.

where the transport distribution function $\Xi(E)$ is defined as follows:²⁴

$$\begin{aligned}\Xi(E) &= \frac{1}{W} \sum_{k_{x,y},n} v_n^2(k_x) \tau_n(k_{x,y}) \delta(E - E_n(k_{x,y})) \\ &= \frac{1}{W} \sum_n v_{k_{x,n}}^2(E) \tau_n(E) g_{2D}^n(E).\end{aligned}\quad (2)$$

Here, $v_{k_{x,n}}(E) = \frac{1}{\hbar} \frac{\partial E_n}{\partial k_x}$ is the group velocity in the transport direction, $\tau_n(k_{x,y})$ is the momentum relaxation time of a carrier with in-plane wave number $k_{x,y}$ in subband n , $g_{2D}^n(E_n)$ is the density of states (DOS) for a 2D subband, E_V is the valence band edge, W is the width of the channel, and E_F is the Fermi level.

We use Fermi's Golden rule to extract the momentum relaxation rates. We include scattering due to elastic acoustic phonons (ADP), inelastic optical phonons (ODP), and SRS, and use the full energy dependence for the momentum relaxation times. For computational efficiency, we make the following approximations: (i) Confinement of phonons is neglected, and dispersionless bulk phonons are assumed. Instead, enhanced deformation potential values $D_{ODP}^{holes} = 13.24 \times 10^{10}$ eV/m and $D_{ADP}^{holes} = 5.34$ eV are employed, as is common practice for nanostructures.^{19,21,25,26} Such treatment could only affect our results quantitatively.²⁷ Our purpose, however, is to provide qualitative insight and design directions. (ii) Surface relaxation is neglected. (iii) For SRS, we assume a 2D exponential autocorrelation function for the roughness with $\Delta_{rms} = 0.48$ nm and $L_C = 1.3$ nm and derive the transition rate from the shift in the band edges $\Delta E_V / \Delta W$ with confinement. As discussed by Uchida *et al.*,²⁸ this is the strongest contribution to SRS in channels of a few nanometers in thickness. All these approximations are commonly employed in numerical calculations. Although in certain cases they might be quite strong, it is believed that they affect the results only quantitatively. Qualitatively, our results are determined mostly by the geometry-dependent electronic structure, which is the main focus of this work. The method is an extension to 2D of what we describe in Ref. 23 for 1D nanostructures.

III. RESULTS AND DISCUSSION

Before we describe the results obtained using the proper atomistic bandstructures, it is useful to estimate how the electronic structure affects σ and S using the simplified parabolic band approximation. For this, we assume $\tau_n(E) \propto W / g_{2D}^n(E)$ and $v_n(E) \propto \sqrt{\tilde{E} / m_{\parallel}^*}$, where $\tilde{E} = E - E_V$, and m_{\parallel}^* is the transport effective mass. We substitute these into Eq. (1), and after performing the summation over the subbands in Eq. (2) (assuming single subband),

$$\sigma \propto \int_{E_V}^{\infty} \tilde{E} / m_{\parallel}^* \left(-\frac{\partial f(E - E_F)}{\partial E} \right) dE = \frac{1}{m_{\parallel}^*} \tilde{I}(\eta_F) \propto \nu_{inj}^2 \tilde{I}(\eta_F), \quad (3)$$

where ν_{inj} is the carrier injection velocity, and $\tilde{I}(\eta_F)$ is a function of $\eta_F = E_V - E_F$, independent of bandstructure at

first order, and *exponentially* increasing with decreasing η_F . Similarly, from Eq. (1b), the Seebeck coefficient S can be shown to follow

$$S \propto \frac{\int_{E_V}^{\infty} F(\eta_F) \left(\frac{E - E_F}{k_B T} \right) dE}{\int_{E_V}^{\infty} F(\eta_F) dE}, \quad (4)$$

where $F(\eta_F) = \tilde{E} \left(-\frac{\partial f(E - E_F)}{\partial E} \right)$ appears in the numerator and denominator. The energy dependence of S is, therefore, at first order independent of bandstructure.²⁹ Its magnitude reduces *linearly* as the subband energy is closer to the Fermi level (smaller η_F), as expected. At a certain carrier concentration, η_F will depend on the DOS of the dispersion (or the DOS effective mass, m_{DOS}). A large DOS will result in larger η_F and larger S , but it will exponentially decrease σ .

The power factor σS^2 , therefore, depends on ν_{inj} and η_F . In UTB layers at a certain carrier concentration, these two quantities are geometry dependent. Figure 1(a) shows the atomistically calculated hole ν_{inj} and η_F for UTB layers on (100), (110), and (112) confinement surfaces, and in [100],

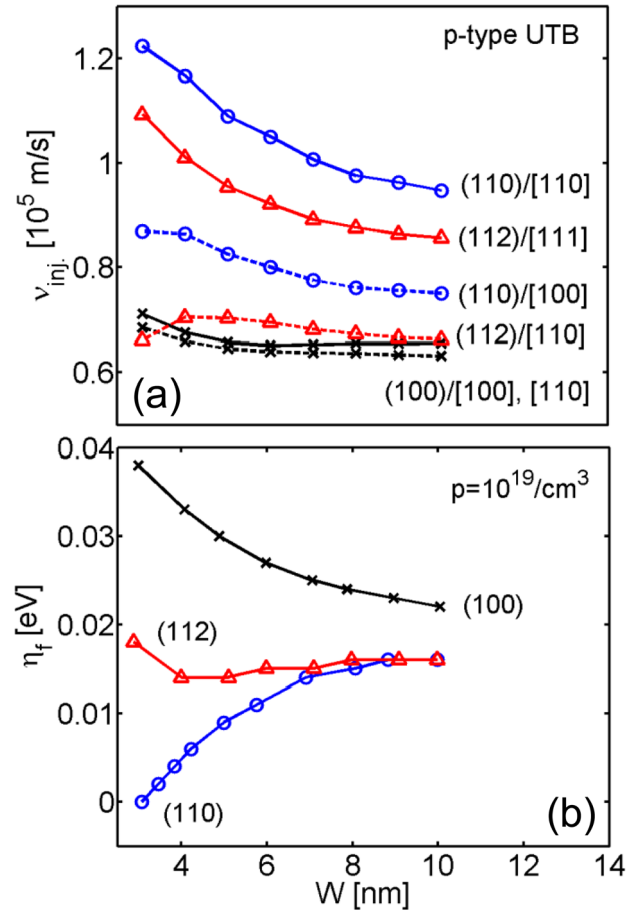


FIG. 1. (a) The carrier injection velocity of the UTB layers vs. the layer thickness W . Channels of various confinement and transport orientations are shown. (b) The $\eta_F = E_V - E_F$ vs. W for the various surfaces. Carrier concentration $p = 10^{19}/\text{cm}^3$ is assumed for all cases.

[110], and [111] transport orientations as a function of the UTB film thickness, W . A hole concentration of $p = 10^{19}/\text{cm}^3$ is assumed (a value close to where the peak of σS^2 appears, as we show below). Strong anisotropic behavior is observed with respect to both surface and transport orientations. The (110)/[110] and (112)/[111] channels provide the highest velocities, followed by the (110)/[100] channel, whereas the (100) surfaces and the (112)/[110] channel have the lowest velocities. As the thickness of the UTB is scaled down, the hole velocities increase, especially for the first two channels. The reasons behind this are related to their bandstructure, and particularly how the curvature of the heavy-hole band along these directions changes under confinement. We will briefly explain this behavior below. The change in the bandstructure with confinement and orientation also results in different DOS for each channel, which changes η_F as well. Figure 1(b) shows the η_F for the three surfaces with respect to the UTB layer thickness, at the same hole concentration of $p = 10^{19}/\text{cm}^3$ for all channels. At larger thicknesses, η_F is very similar in all cases because the films are thick enough for the DOS to approach the bulk DOS in all cases. As the UTB layer thickness is reduced, the η_F for the (110) surface decreases. The η_F in the (112) surface layers remains almost unchanged, whereas in the case of the (100) surface layers, η_F increases.

The behavior of the η_F as a function of surface orientation and layer width originates for the bandstructure of the channels, and how this changes with confinement and orientation. We provide an elaborate discussion regarding the bandstructures of thin p-type layers as well as nanowires in Refs. 16, 17, 30, 31 and we refer the reader to those works for details. Here, we only provide a brief discussion on how these changes will affect η_F . Figure 2(a) shows the DOS(E) for (110) surface channels of widths $W = 10\text{ nm}$ and $W = 3\text{ nm}$. Both functions are shifted to the same origin for comparison purposes. The insets show the corresponding bandstructures with the arrows pointing to the [110] direction. As the width is reduced, the bandstructure in the [110] direction acquires a larger curvature. The bands become lighter, which justifies the velocity increase in Fig. 1(a) for the (110)/[110] channel. The lighter bands, however, also result in smaller DOS(E) for the thinner UTB layer as shown in Fig. 2(a). At a constant carrier concentration, the reduction in the DOS(E) will reduce η_F as the width of the channel is reduced. The Fermi level will shift closer to the band edge in order to keep the carrier concentration constant. The situation is reversed for the (100) surface channels. Figure 2(b) shows the DOS(E) for the (100) channels of widths $W = 10\text{ nm}$ and $W = 3\text{ nm}$. The electronic structure of these channels does not change significantly with confinement as shown by the insets of Fig. 2(b). This is also reflected by the constant carrier velocities with width of the (100)/[100] and (100)/[110] channels in Fig. 1(a). The 3D DOS(E) in this case, however, increases with confinement after the normalization by the width W . Assuming a simple effective mass approximation, the DOS is proportional to M/W , where M is the number of subbands and W is the normalization width of the thin layer. As the width is reduced, the number of subbands M decreases, usually linearly for the thicker layers

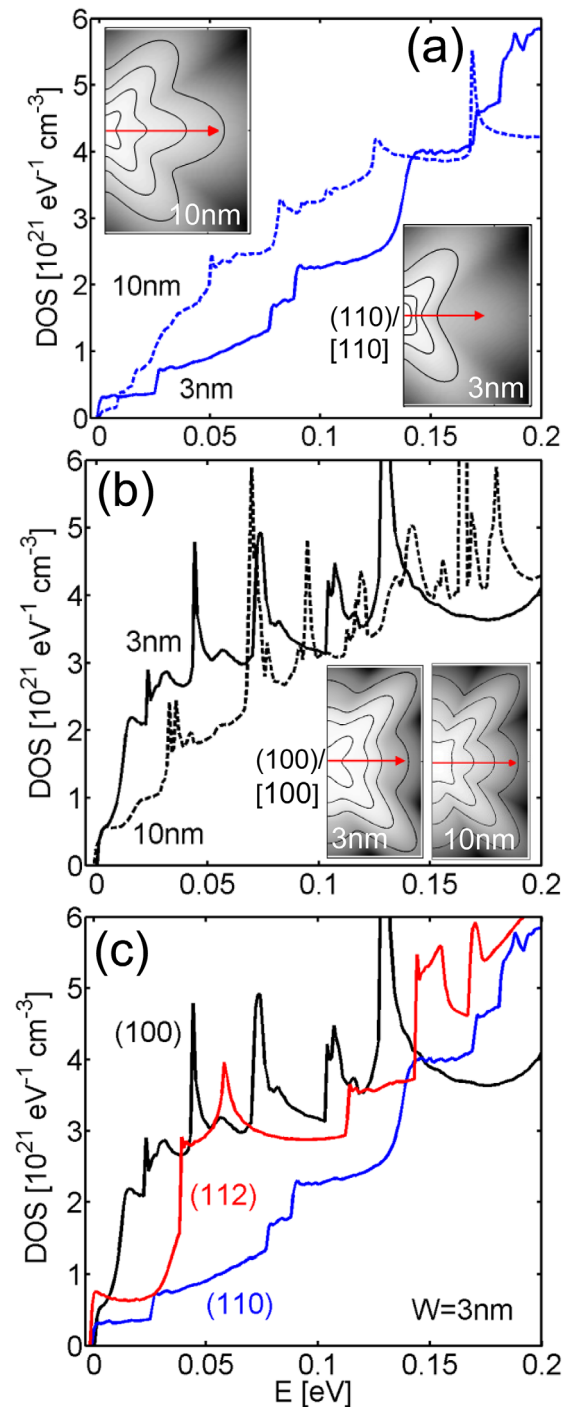


FIG. 2. The DOS versus energy for UTB layers of different widths on different surfaces. (a) (110) surface and widths $W = 3\text{ nm}$ (solid) and $W = 10\text{ nm}$ (dashed). (b) (100) surface and widths $W = 3\text{ nm}$ (solid) and $W = 10\text{ nm}$ (dashed). Insets of (a) and (b): the corresponding $E(k)$ energy surfaces for the highest subbands. (c) The DOS(E) versus energy for the (100), (110), and (112) surfaces of the channels with $W = 3\text{ nm}$.

such that the ratio M/W remains constant. At some point, only a few or even only one subband participates in transport. Further reduction of the width of the UTB layer will not be linearly compensated by a reduction in M , and the ratio M/W will increase following $\sim 1/W$ as M approaches closer to 1. The DOS(E), therefore, increases with confinement. Since the carrier concentration under a simple effective mass approximation is given by

$$n_{3D} = \frac{M}{W} \int_{E_V}^{\infty} g_{2D}(E) f(E - E_F) dE, \quad (5)$$

in order to keep the carrier concentration n_{3D} constant, the energy integral has to be reduced, which is achieved when the distance of the subband edges E_V from the Fermi level $\eta_F = E_V - E_F$ is increased. The η_F then increases as observed in Fig. 1(b).

The larger the $\text{DOS}(E)$, therefore, the larger the η_F at a certain carrier concentration. Figure 2(c) shows the $\text{DOS}(E)$ for the $W = 3$ nm thin layers of (100), (112), and (110) surfaces. The $\text{DOS}(E)$ of the (100) layer is the largest, followed by that of the (112) layer, whereas that of the (110) layer is the smallest. Indeed, this follows the order in which η_F appears in Fig. 1(b).

The v_{inj} and η_F will determine σ and S for the UTB layers. Figure 3(a) shows the phonon-limited conductivity of the UTB channels as a function of the layer thickness W at $p = 10^{19}/\text{cm}^3$. Clearly, the (110)/[110] channel is advantageous compared to the other channels considered at all thicknesses. It is especially superior at smaller thicknesses, for which the conductivity of this channel largely improves (by $\sim 3\times$), whereas that of the other channels shows either only slight improvement, or even slight degradation. This advantage of [110] p-type channels under strong (110) confinement is also verified by recent mobility measurements.^{32–35} This difference in performance between the different orientations originates from the fact that the (110)/[110] channels not only have the highest carrier velocities but at the same carrier concentration they have the smallest η_F . Both quantities benefit the conductivity. On the other hand, the $\sim 3\times$ increase in σ with thickness scaling for this channel can be justified from Eq. (3) by comparing σ in the $W = 3$ nm and 10 nm UTB channels:

$$\frac{\sigma_{3\text{nm}}}{\sigma_{10\text{nm}}} \propto \frac{\nu_{inj-3\text{nm}}^2}{\nu_{inj-10\text{nm}}^2} \frac{\tilde{I}(\eta_F)}{\tilde{I}(\eta_F + \Delta\eta_F)} \approx \left(\frac{1.22}{0.94}\right)^2 e^{\Delta\eta_F/k_B T} = 3.11, \quad (6)$$

where $\Delta\eta_F = 0.16$ eV (from Fig. 1(b)).

The dependence of the Seebeck coefficient on the layer thickness in Fig. 3(b) follows the dependence of η_F on thickness, as also explained above in Eq. (4). At larger thicknesses, S is very similar for all channels. As the thickness is reduced, S decreases in the (110) layers by $\sim 30\%$, slightly decreases in the (112) layers, and increases in the (100) layers.

Since the σ depends exponentially on η_F as shown in Eqs. (3) and (6), the power factor is more controlled by the electrical conductivity. The power factor trend with W in Fig. 3(c) is very similar to the conductivity trend in Fig. 3(a). The (110)/[110] channel outperforms the rest of the channels by more than $2\times$ in the entire range of the examined thicknesses, despite the fact that S decreases for that channel at smaller thicknesses. In fact, the power factor increases by $\sim 40\%$ as the layer thickness is decreased. The performance of all other channels is lower and very similar to each other.

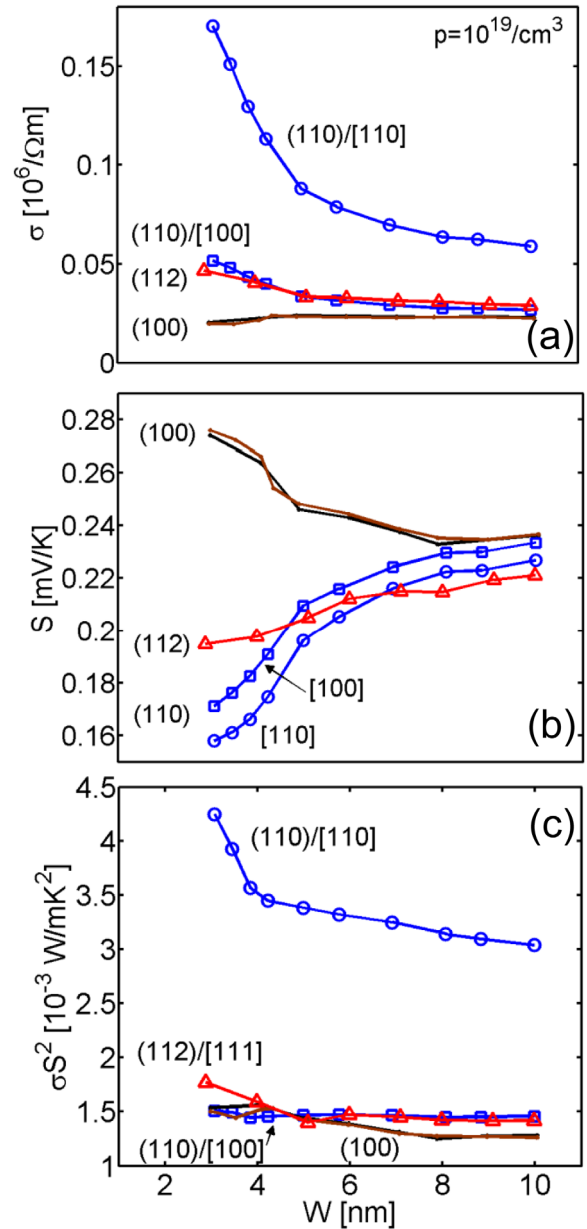


FIG. 3. Phonon-limited thermoelectric coefficients for p-type UTB layers at $p = 10^{19}/\text{cm}^3$ versus layer thickness W : (a) electrical conductivity, (b) Seebeck coefficient, and (c) power factor. Various surface and transport orientations are presented as noted.

We note here that the orientation dependence of the power factor in p-type UTB layers does not have a one-to-one correspondence to that of p-type NWs presented in Ref. 23. For the NWs, we showed that the [111] direction performs better than the [110] direction because of the lighter subbands that improve conductivity and reduce η_F . In the case of UTB layers, however, although the [111] oriented channel has high velocities, η_F remains larger because of the higher DOS (Fig. 2(c)), resulting in reduced conductivity and power factor.

The large performance advantage for the (110)/[110] channel compared to the other channels is attributed to its larger electrical conductivity σ . It is not only larger in this channel compared to the rest but it additionally increases for

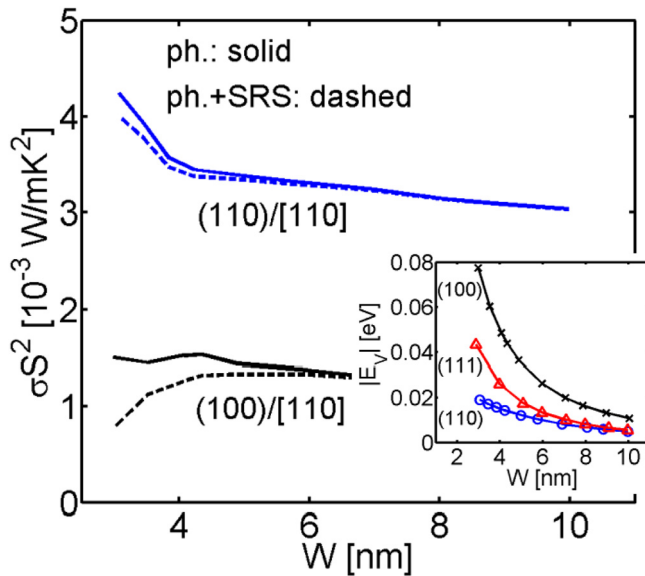


FIG. 4. Power factor for p-type UTB layers at $p = 10^{19}/\text{cm}^3$ versus layer thickness W . [110] transport channels on (110) and (100) surfaces are presented as noted. Solid lines: phonon-limited results. Dashed lines: phonon plus SRS limited results. Inset: the valence band edges of the (100), (110), and (112) surfaces versus W .

thinner channel widths. In reality, however, σ deteriorates in nanostructures due to enhanced SRS. In Fig. 4, we include SRS in the calculations for $\sigma\sigma^2$ (dashed lines). We assume that the influence of SRS originates from the shift in the band edges of the channel dispersions.²⁸ The inset of Fig. 4 shows the band edges for the (110), (112), and (100) surfaces with respect to the layer thickness. The band edge in (110) films is the one affected the least, whereas the band edge in (100) films is the one affected the most by layer thickness fluctuations. This is an indication of a heavy confinement effective mass for the (110) surface, and a light one for the (100) surface.

The power factor in Fig. 4 is reduced once SRS is considered (here only results for the (110) and (100) surfaces in [110] transport are shown). The reduction originates solely from the reduction in σ because the Seebeck coefficient is at first order independent of scattering, and it only marginally increases with SRS (Ref. 23). In the case of the (110) surface, SRS affects the conductivity and in extent the power factor only slightly, because of the weak shift in the band edges with confinement. The effect of SRS is stronger for the (100) surface, where the band edges are more sensitive to confinement. The (110)/[110] channel, therefore, not only outperforms the other channels but it can also provide larger immunity to SRS. Thus, it can be the ideal candidate for p-type UTB layer thermoelectrics and possibly 2D in-plane superlattice thermoelectric materials. Quantitatively, the strength of SRS is determined by the roughness height Δ_{rms} , and might possibly be stronger once additional Coulomb related effects are considered.³⁶ The point, however, is that the (110)/[110] channel, with the larger confinement effective mass, and the underlying bandstructure mechanism that causes the conductivity and the power factor to increase with thickness reduction, can compensate the detrimental effects of SRS. This is particularly

important, because small feature sizes and roughness are necessary in order to achieve a large reduction in κ_l and enhance the ZT figure of merit. For this purpose, rough nanowires,^{4,5} thin-layers,⁶⁻⁹ and lately nanoporous materials^{10,14} are currently receiving large attention. Such approaches, however, often degrade the power factor as well. The confinement and orientation dependences we describe provide guidance into how to still achieve high power factors in such channels, necessary for enhanced thermoelectric performance, and how to partially compensate for detrimental roughness and distortion effects.

A comparison between the performance of the p-type (110)/[110] UTB layers presented here, and the p-type [110] NWs we present in Ref. 23, shows that the stronger confinement in [110] NWs could provide somewhat larger power factors at narrower diameters of 3 nm. However, [110] NWs suffer more from SRS because they are also confined by the strongly affected (100) surface, rather than only the weakly affected (110) surface. Once SRS is considered, the performance of the two channels is very similar. 2D thin layers, however, could offer the advantage of being more easily scaled to industrial processes than 1D NWs. Besides, the thermal conductivity in 2D layers can be as low as the one achieved in NWs for such small feature sizes. In recent works, it was shown both by experiments and simulations that 2D thin layers, nanoporous thin films of Si or SiGe,^{10,14,37} and 2D superlattices composed of Si layers/Ge nanodots¹⁵ could have thermal conductivities close to or even below the amorphous limit. Furthermore, it was shown that in some of these structures the electron transport is much less disrupted. This means that proper power factor optimization as we suggest in this work, not only in thin films but also in the thin-film-based structures we mention above, could potentially provide high ZT values at room temperature as well, similar to what has been measured in NWs.^{4,5}

The UTB orientation comparison as of now was limited to a fixed carrier concentration of $p = 10^{19}/\text{cm}^3$. We show

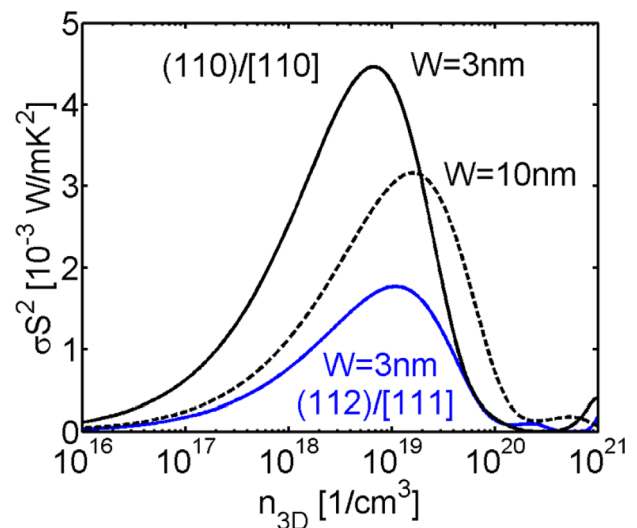


FIG. 5. The phonon-limited thermoelectric power factor for UTB layers vs. the carrier concentration. UTB channels shown: (i) (110)/[110] with $W = 3 \text{ nm}$ (solid-black), (ii) (110)/[110] with $W = 12 \text{ nm}$ (dashed-black), and (iii) (112)/[111] with $W = 3 \text{ nm}$ (solid-blue).

here, however, that the performance advantage of the (110)/[110] channel holds for different hole concentrations as well. In Fig. 5, we show the phonon-limited power factor as a function of the carrier concentration for three different channels, the (110)/[110] channel with (i) $W=3$ nm and (ii) $W=10$ nm, and (iii) the (112)/[111] channel with $W=3$ nm. The rest of the channels have similar or lower power factors than the (112)/[111] channel, at least for carrier concentrations below $p=10^{20}/\text{cm}^3$. For the sake of clarity, we do not show them here. The (110)/[110] channel has a higher power factor in the entire carrier concentration range. For these orientations, the thinner $W=3$ nm channel has a higher σS^2 up to concentrations of $p=10^{19}/\text{cm}^3$, whereas at higher concentrations it loses this advantage to the thicker layer of the same channel orientation. Note, however, that it has the highest maximum power factor compared to the other layers, which peaks around carrier concentrations $p=7 \times 10^{18}/\text{cm}^3$.

IV. CONCLUSION

In summary, we have calculated the thermoelectric coefficients (σ , S , σS^2) for silicon p-type ultra-thin-body layers with channel thicknesses from $W=3$ nm to $W=10$ nm using atomistic electronic structure and Boltzmann transport calculations. We have investigated various transport and confinement orientations. We find that the (110)/[110] channel shows a significant performance advantage compared to all other channel orientations (by more than $2\times$), and in addition, the phonon-limited power factor in such channel increases by $\sim 40\%$ as the (110) confinement increases. Furthermore, the (110) surface shows stronger immunity to the detrimental effect of SRS because of a larger confinement effective mass. These factors make the (110)/[110] channel an ideal candidate for ultra-thin p-type thermoelectric channels. Quantitatively, this conclusion is relevant not only for Si but for other zincblende p-type materials with similar valence band features as well. Our results could provide guidance into design optimization strategies for high power factor in low-dimensional and nanostructured thermoelectric devices, in which narrow feature sizes are necessary to reduce the phonon part of the thermal conductivity κ_l to achieve enhanced ZT figure of merit.

ACKNOWLEDGMENTS

This work was supported by the Austrian Climate and Energy Fund, Contract No. 825467.

¹A. Majumdar, *Sci. Mater.* **303**, 777–778 (2004).

²G. J. Snyder and E. S. Toberer, *Nat. Mater.* **7**, 105–114 (2008).

- ³K. Nielsch, J. Bachmann, J. Kimling, and H. Boettner, *Adv. Energy Mater.* **1**, 713–731 (2011).
- ⁴A. I. Hochbaum, R. Chen, R. D. Delgado, W. Liang, E. C. Garnett, M. Najarian, A. Majumdar, and P. Yang, *Nature* **451**, 163–168 (2008).
- ⁵A. I. Boukai, Y. Bunimovich, J. T. Kheli, J.-K. Yu, W. A. Goddard III, and J. R. Heath, *Nature* **451**, 168–171 (2008).
- ⁶R. Venkatasubramanian, E. Siivola, T. Colpitts, and B. O'Quinn, *Nature* **413**, 597–602 (2001).
- ⁷W. Kim, S. L. Singer, A. Majumdar, D. Vashaee, Z. Bian, A. Shakouri, G. Zeng, J. E. Bowers, J. M. O. Zide, and A. C. Gossard, *Appl. Phys. Lett.* **88**, 242107 (2006).
- ⁸D. Li, Y. Wu, R. Fang, P. Yang, and A. Majumdar, *Appl. Phys. Lett.* **83**(15), 3186–3188 (2003).
- ⁹G. Zeng, J. E. Bowers, J. M. O. Zide, A. C. Gossard, W. Kim, S. Singer, A. Majumdar, R. Singh, Z. Bian, Y. Zhang, and A. Shakouri, *Appl. Phys. Lett.* **88**, 113502 (2006).
- ¹⁰J. Tang, H.-T. Wang, D. H. Lee, M. Fardy, Z. Huo, T. P. Russell, and P. Yang, *Nano Lett.* **10**, 4279–4283 (2010).
- ¹¹C. J. Vineis, A. Shakouri, A. Majumdar, and M. C. Kanatzidis, *Adv. Mater.* **22**, 3970–3980 (2010).
- ¹²R. Chen, A. I. Hochbaum, P. Murphy, J. Moore, P. Yang, and A. Majumdar, *Phys. Rev. Lett.* **101**, 105501 (2008).
- ¹³P. Martin, Z. Aksamija, E. Pop, and U. Ravaioli, *Phys. Rev. Lett.* **102**, 125503 (2009).
- ¹⁴Y. He, D. Donadio, and G. Galli, *Nano Lett.* **11**(9), 3608–3611 (2011).
- ¹⁵G. Pernot *et al.*, *Nat. Mater.* **9**, 491–495 (2010).
- ¹⁶N. Neophytou and H. Kosina, *Nano Lett.* **10**(12), 4913–4919 (2010).
- ¹⁷N. Neophytou, G. Klimeck, and H. Kosina, *J. Appl. Phys.* **109**, 053721 (2011).
- ¹⁸N. Neophytou and H. Kosina, *Phys. Rev. B* **84**, 085313 (2011).
- ¹⁹H. J. Ryu, Z. Aksamija, D. M. Paskiewicz, S. A. Scott, M. G. Lagally, I. Knezevic, and M. A. Eriksson, *Phys. Rev. Lett.* **105**, 256601 (2010).
- ²⁰T. B. Boykin, G. Klimeck, and F. Oyafuso, *Phys. Rev. B* **69**, 115201 (2004).
- ²¹A. K. Buin, A. Verma, and M. P. Anantram, *J. Appl. Phys.* **104**, 053716 (2008).
- ²²V. M. Fomin and P. Kratzer, *Phys. Rev. B* **82**, 045318 (2010).
- ²³N. Neophytou and H. Kosina, *Phys. Rev. B* **83**, 245305 (2011).
- ²⁴T. J. Scheidmantel, C. A. Draxl, T. Thonhauser, J. V. Badding, and J. O. Sofo, *Phys. Rev. B* **68**, 125210 (2003).
- ²⁵M. V. Fischetti and S. E. Laux, *J. Appl. Phys.* **80**, 2234 (1996).
- ²⁶T. Yamada and D. K. Ferry, *Solid-State Electron.* **38**, 881 (1995).
- ²⁷L. Donetti, F. Gamiz, N. Rodriguez, and A. Godoy, *IEEE Electron Device Lett.* **30**(12), 1338 (2009).
- ²⁸K. Uchida and S. Takagi, *Appl. Phys. Lett.* **82**, 2916 (2003).
- ²⁹R. Kim, S. Datta, and M. S. Lundstrom, *J. Appl. Phys.* **105**, 034506 (2009).
- ³⁰N. Neophytou, A. Paul, and G. Klimeck, *IEEE Trans. Nanotechnol.* **7**, 710 (2008).
- ³¹N. Neophytou and H. Kosina, *Solid State Electron.* **70**, 81–91 (2012).
- ³²K. Trivedi, H. Yuk, H. C. Floresca, M. J. Kim, and W. Hu, *Nano Lett.* **11**, 1412 (2011).
- ³³M. Yang, V. W. C. Chan, K. K. Chan, L. Shi, D. M. Fried, J. H. Stathis, A. I. Chou, E. Gusev, J. A. Ott, L. E. Burns, M. V. Fischetti, and M. Jeong, *IEEE Trans. Electron Device* **53**, 965 (2006).
- ³⁴J. Chen, T. Saraya, and T. Hiramoto, *IEEE Electron Device Lett.* **31**, 1181 (2010).
- ³⁵G. Tsutsui, M. Saitoh, and T. Hiramoto, *IEEE Electron Device Lett.* **26**, 836 (2005).
- ³⁶S. Jin, M. Fischetti, and T.-W. Tang, *IEEE Trans. Electron Device* **54**, 2191 (2007).
- ³⁷J.-H. Lee, G. A. Galli, and J. C. Grossman, *Nano Lett.* **8**(11), 3750–3754 (2008).